ACS APPLIED NANO MATERIALS
Cite This: ACS Appl. Nano Mater. 2019, 2, 3684−3694
Article
www.acsanm.org

Large Metallic Vanadium Disulfide Ultrathin Flakes for Spintronic Circuits and Quantum Computing Devices

Aaron J. Littlejohn,[*,†,‡] Zhaodong Li,[†] Zonghuan Lu,[‡] Xin Sun,[‡] Poomirat Nawarat,[†] Yiping Wang,[§] Yang Li,[∥] Tianmeng Wang,[∥] Yanwen Chen,[∥] Lihua Zhang,[#] Hongxia Li,[%] Kim Kisslinger,[#] Sufei Shi,[∥,⊥] Jian Shi,[§] Aldo Raeliarijaona,[†] Wenqing Shi,[&] Humberto Terrones,[†] Kim M. Lewis,[†,‡] Morris Washington,[†,‡] Toh-Ming Lu,[†,‡] and Gwo-Ching Wang[†,‡]

[†]Department of Physics, Applied Physics and Astronomy, [‡]Center for Materials, Devices, and Integrated Systems, [§]Department of Materials Science and Engineering, [∥]Department of Chemical and Biological Engineering, and [⊥]Department of Electrical, Computer and Systems Engineering, Rensselaer Polytechnic Institute, 110 Eighth Street, Troy, New York 12180, United States

[#]Center for Functional Nanomaterials, Brookhaven National Laboratory, Upton, New York 11973, United States

[%]College of Materials and Environmental Engineering, Hangzhou Dianzi University, Hangzhou 310018, People's Republic of China

[&]Park Systems, Inc., Santa Clara, California 95054, United States

Supporting Information

ABSTRACT: Atmospheric pressure chemical vapor deposition (APCVD) is employed for the synthesis of layered vanadium disulfide. By tuning several critical growth parameters, we achieve VS_2 flakes with lateral dimension over 100 μm and thickness down to monolayer (~0.59 nm) and bilayer (~1.17 nm), which are larger and thinner than those previously reported in the literature. Furthermore, ultrathin flakes with thicknesses of several atomic layers are directly synthesized on mica and SiO_2 substrates without the use of an exfoliation method. X-ray diffraction and high-resolution transmission electron microscopy confirm the flakes' monocrystalline quality. Raman spectra are collected and are consistent with the vibrational modes for the trigonal phase of VS_2 as determined by density functional theory calculations. Through electron backscatter diffraction pole figure analysis, transmission electron microscopy, and optical microscopy, a complex epitaxial relationship with nine preferred in-plane orientations is observed in some regions of the VS_2/mica samples. Remarkably, this is in agreement qualitatively with a superlattice area mismatch model, providing further evidence of the interfacial interactions with mica dictating the nucleation of film atoms in van der Waals heterostructures. Finally, magnetic force microscopy measurements suggest room-temperature ferromagnetism in ultrathin VS_2 flakes, in agreement with several density functional theory calculations. The discovery of an ultrathin ferromagnetic metal such as VS_2 may have an impact on emerging fields such as spintronics and quantum computing.

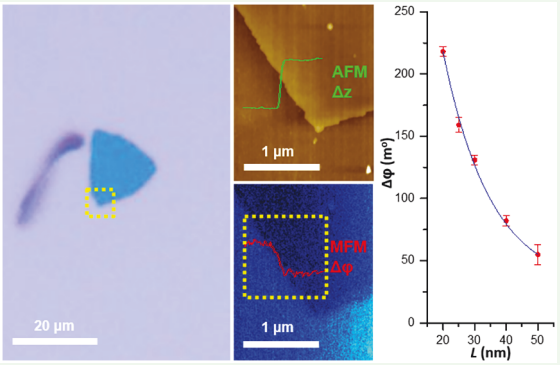

KEYWORDS: *2D materials, transition metal dichalcogenides, van der Waals epitaxy, heteroepitaxy, chemical vapor deposition, ferromagnetism*

INTRODUCTION

Over the past decade, two-dimensional (2D) materials have received a tremendous surge of interest due to their intriguing mechanical, electronic, and optical properties.[1] Even more recently, the exploration of ferromagnetism in 2D materials is an area of research attracting great attention. If the aforementioned properties could be endowed with ferromagnetism, it would enable the development of next-generation 2D magnetic, magnetoelectric, and magneto-optic devices. Many layered compounds containing ferromagnetic elements such as $Cr_2Ge_2Te_6$ and halides including CrI_3 have intrinsic magneto-crystalline anisotropy in their bulk form and were shown decades ago to have magnetic properties with a Curie temperature below room temperature.[2] These van der Waals (vdW) magnetic crystals consist of a stacking of vdW interacted 2D crystalline layers.[2−7] However, when the thickness of the vdW magnetic crystal is reduced and the crystal transitions to the 2D format, strong thermal fluctuations at finite temperature were believed to prohibit 2D ferromagnetism according to the Mermin−Wagner theorem,[8] leading to a fundamental challenge in obtaining long-range ferromagnetic order in the 2D regime. In 2017, substantial progress was made

Received: April 2, 2019
Accepted: May 20, 2019
Published: May 22, 2019

DOI: 10.1021/acsanm.9b00608
ACS Appl. Nano Mater. 2019, 2, 3684−3694

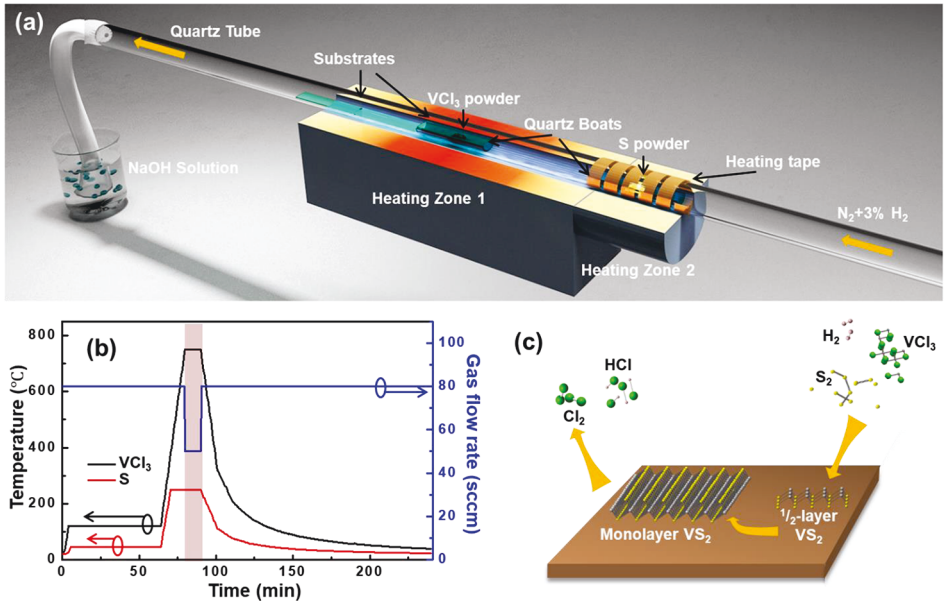

Figure 1. (a) Schematic of atmospheric pressure chemical vapor deposition growth setup. (b) Zone I temperature (black curve), zone II temperature (red curve), and gas flow rate (blue curve) during VS_2 synthesis. (c) Schematic of chemical precursors, synthesized compounds, and products.

by magneto-optical Kerr effect microscopy characterizations, which revealed the stable long-range ferromagnetic ordering down to atomic layer $Cr_2Ge_2Te_6$[9] and CrI_3 flakes with Curie temperatures below room temperature and lower than their bulk Curie temperatures.[4]

Another category of widely studied vdW 2D crystals is graphene and transition metal dichalcogenides (TMDCs), which have shown many fascinating mechanical and electronic properties. However, few magnetism studies have been conducted because their corresponding bulk crystals are typically nonmagnetic. Therefore, three practical methods have been designed to extrinsically induce magnetism within these 2D materials, including defect engineering (vacancies,[10] adatoms, and grain boundaries), magnetic element doping,[11] and structural phase transitioning.[12] Nevertheless, the very localized and limited magnetic moments generated by such routes are not stable or controllable enough to fabricate devices. Achieving intrinsic room temperature ferromagnetism originating from these vdW 2D crystals will be crucial for understanding the physics of electronic and spin processes and for device applications. Recent density functional theory (DFT) calculations have predicted the intrinsic magnetic moment (~0.5−1 μ_B) of monolayer (ML) metallic vanadium disulfide (VS_2), which can be tuned either by varying the number of layers or by applying biaxial tensile/isotropic strain.[13−20] Zigzag-type VS_2 nanoribbons are also intrinsically ferromagnetic depending on the edge structure.[21] Furthermore, exploration using a superconducting quantum interference device (SQUID) magnetometer has suggested temperature-dependent ferromagnetism in wet hydrothermally synthesized nanosheets as well as vacuum-cleaved and powdered VS_2.[15,22,23] A dramatic decrease in magnetization or susceptibility was observed as the temperature increased from 10 K to room temperature. By exfoliating the VS_2 nanosheets to a few layers, one could observe magnetic hysteresis loops at 300 K.[15,24,25] In addition, the investigation of magnetic properties of other common V−S compounds such as V_5S_8 also has been carried out.[26,27]

Unfortunately, because of the wet-chemical synthesis processes which have predominantly induced defects and lacked composition and thickness control, such ferromagnetism is difficult to correlate to the intrinsic property of VS_2. In addition, the theoretical calculations consider ultrathin to ML free-standing single crystal VS_2 and do not consider any effect from the substrate, whereas experimentally most polycrystalline VS_2 nanostructures were grown either directly on a substrate, or in a solution and subsequently transferred to a substrate. The interaction between the VS_2 and the substrate induced uneven orientations and strain within the VS_2. No experimental evidence yet exists for ferromagnetism observation in VS_2 persisting down to the 2D single crystal limit. One extremely encouraging work on well-characterized monolayer VSe_2 islands was reported to have room temperature ferromagnetism[28] (note that bulk VSe_2 is paramagnetic). The monolayer VSe_2 islands were grown by electron beam evaporation of V and simultaneous deposition of atomic Se on either highly orientated pyrolytic graphite (HOPG) or MoS_2 substrates in an ultrahigh vacuum environment.

Very recently, monolayer VS_2 has been successfully grown on Au(111) by e-beam evaporation of V rod or V wire and annealed in sulfiding gas (either H_2S or dimethyl disulfide) under ultrahigh vacuum (UHV).[29] In contrast to the growth of VS_2 in UHV, the chemical vapor deposition (CVD) technique has successfully achieved single-crystal ultrathin VS_2 flakes on SiO_2 substrates.[30,31] CVD has also been utilized to realize the epitaxial growth of strain-free 2D materials on vdW substrates such as graphene.[32,33] We thus expect the film/substrate interaction to be much weaker when VS_2 is grown on a single crystal vdW material, such as muscovite mica (potassium aluminosilicate), as compared to growth on a bulk amorphous substrate, such as SiO_2. In this work, we report the growth of large (several tens to hundreds of micrometers in diameter), ultrathin (several ML) crystalline VS_2 flakes with good stoichiometry on single-crystal vdW mica and amorphous SiO_2/Si(100) substrates via the atmospheric pressure chemical vapor deposition (APCVD) technique. Each VS_2 flake has a

DOI: 10.1021/acsanm.9b00608
ACS Appl. Nano Mater. 2019, 2, 3684−3694

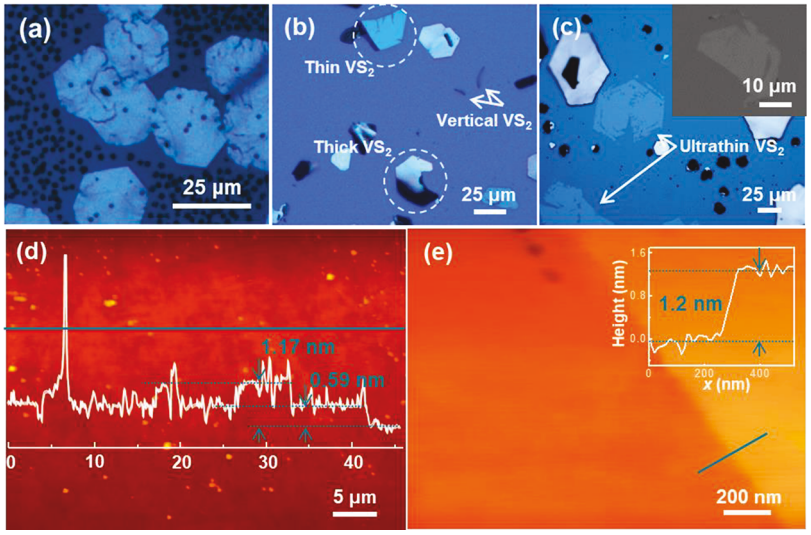

Figure 2. (a) Optical image of VS_2 flakes grown on single crystal mica(001) in region directly above VCl_3 boat. (b, c) Optical images showing different morphologies of VS_2 flakes grown on amorphous SiO_2. Inset of (c): SEM image of an ultrathin flake. (d, e) AFM images of ultrathin flakes with monolayer and bilayer step edges on SiO_2.

well-defined out-of-plane (001) orientation while the in-plane orientation of VS_2 flakes is governed by the interfacial interactions of VS_2 and the mica (001) surface. This observation agrees with a superlattice area mismatch model. In addition, magnetic force microscopy (MFM) measurements that suggest room temperature ferromagnetism in ultrathin VS_2 flakes are presented. These findings enhance our fundamental knowledge of epitaxy in 2D/2D materials systems and magnetism in the 2D limit.

RESULTS AND DISCUSSION

A dual-zone APCVD setup was utilized for the synthesis of large thin to ultrathin VS_2 flakes (details in the Methods section), depicted schematically in Figure 1a. The critical synthesis factors were the deposition temperature, precursor-vapor concentrations, and carrier gas to form the 2D flakes with a certain stoichiometry. The precursor boats containing S and VCl_3 powders and the substrates (mica or SiO_2/Si) were arranged successively within a quartz tube and mounted in a furnace with a controllable temperature for each precursor and substrate. Forming gas (3% H_2 in N_2) was used to transport the precursors upon evaporation, meanwhile decomposing the precursor molecules as well as inhibiting the thermally induced etching effect and oxidation in the continuous film growth process.[34−37] Before starting the growth, oxygen and moisture in the S and VCl_3 powders were removed by heating to 50 and 150 °C, respectively, while flushing with forming gas (Figure 1b). A possible reaction was conducted on the substrate at 750 °C for 2D VS_2 flakes formation, assuming that S_2 is the most abundant species in the sulfur vapor[38] (Figure 1c):

$$2VCl_3 + 2S_2 + 3H_2 \rightarrow 2VS_2 + 6HCl \quad (1)$$

Optical microscopy reveals the flakes grown on both mica and SiO_2 substrates exhibit various morphologies such as hexagonal, semihexagonal, and triangular. Figure 2a shows the VS_2 flakes grown under optimal conditions on a mica substrate that was placed face-down on top of the VCl_3 boat. In addition to large tens of micrometers flakes, many smaller, thicker flakes as well as nuclei clusters appear as darker spots on the substrate. Thicker hexagonal flakes can be obtained on mica immediately downstream from the VCl_3 precursor boat. Triangular flakes with smaller thicknesses and lateral sizes are observed farther downstream and shown in Figure S1. In contrast to growth on mica substrates, when grown on SiO_2, shown in Figure 2b, many inclined flakes are observed (i.e., those whose surface normal is not normal to the substrate surface). In addition, despite the imperceptibility of the flakes due to their thinness, some ultrathin flakes with thicknesses below 10 nm can be perceived by adjusting the image setting (Figure 2c) or by scanning electron microscopy (SEM) (Figure 2c, inset). The lateral profiles of the flakes grown on mica and SiO_2 substrates were characterized by atomic force microscopy (AFM). Compared to a thickness of ∼35 nm from a typical triangular flake on mica substrate, a superimposed line profile across the ultrathin flake grown on SiO_2 indicates monolayer (∼0.59 nm) and bilayer (∼1.17 nm) steps (Figure 2d,e), consistent with integer multiples of the lattice constant, c (= 0.576 nm) of VS_2.

Attributed to the fundamentally different surfaces of the two substrates, in that mica exhibits a vdW layered crystal structure while SiO_2 is amorphous, the adatom/substrate interaction is commonly believed to be much weaker when VS_2 is grown on mica than when grown on bulk SiO_2. Such a substrate effect to the 2D VS_2 flakes morphology was investigated by using AFM to measure the flake dimension distributions on these two substrates via a statistical sampling method.[39,40] In general, there is a wide distribution in the lateral sizes of triangular and hexagonal flakes grown on mica, with most flakes on the order of tens of micrometers in size (a histogram of the lateral sizes is shown in Figure S2a). This range of lateral sizes is much wider when the flakes are grown on SiO_2 (Figure S2c). These observations imply the nucleation at the initial CVD growth stage is heterogeneous, and the VS_2 growth on mica is more uniform, which is further evidenced by comparison of the flake thickness histograms of mica and SiO_2 substrates, measured by AFM (Figure S2b,d). Moreover, it is noteworthy that the inhomogeneities of the lateral sizes and thicknesses of the flakes exist even for identical growth conditions on both substrates, implying that there is an energy barrier preventing purely lateral growth.

DOI: 10.1021/acsanm.9b00608
ACS Appl. Nano Mater. 2019, 2, 3684−3694

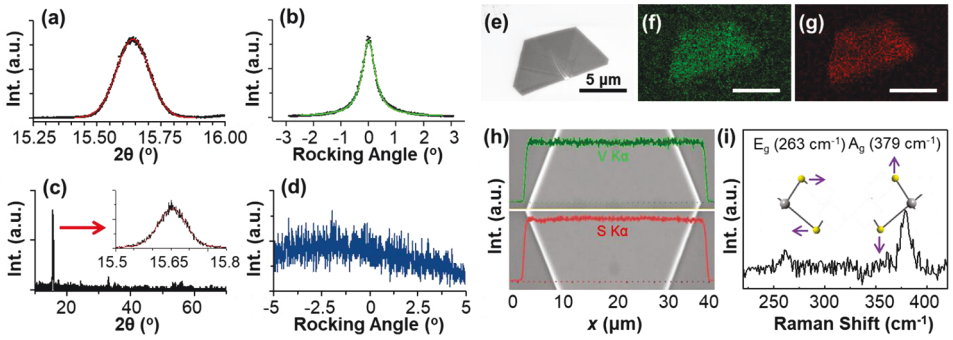

Figure 3. (a, b) XRD of VS_2 flakes grown on mica: (a) θ–2θ; (b) VS_2(001) rocking curve. (c, d) XRD of VS_2 flakes grown on SiO_2: (c) GIXRD (inset: VS_2(001) peak), (d) VS_2(001) rocking curve. (e) SEM image of ultrathin VS_2 flake on SiO_2 with corresponding EDS maps of (f) V Kα and (g) S Kα signals (scale bars = 5 μm). (h) SEM image of VS_2 flake on mica. EDS line scans of V Kα and S Kα are superimposed in green and red, respectively. (i) Raman spectrum of VS_2 flake on SiO_2. Schematics illustrating the observed E_g and A_g modes are superimposed over the corresponding peak.

Nevertheless, the overall growth behavior of the VS_2 still indicates a preference for lateral diffusion over vertical growth with an aspect ratio (lateral dimension/thickness) much larger than one. To explain this, first-principles calculations of the VS_2 (100) and (001) surface energies ($E_{(100)}$ and $E_{(001)}$, respectively) were conducted, and the ratio was calculated therefrom ($E_{(100)}/E_{(001)}$; see details in the Methods section and the Supporting Information). A larger (100)/(001) surface energy ratio is indicative of an inherent proclivity for lateral crystal growth.[41] The estimated $E_{(100)}$ and $E_{(001)}$ surface energies for VS_2 are approximately 2.62 and 0.143 J cm^{-2}, respectively, giving a ratio of ~18.3. Compared to an extensively studied TMDC material such as MoS_2, which is commonly grown in ultrathin-to-monolayer form on various substrates by CVD, this value for VS_2 is much smaller (our calculation yields 2.81 J cm^{-2}/0.106 J cm^{-2} ~ 26.5 for MoS_2). Such a comparison may indicate achieving large ultrathin VS_2 flakes is more challenging than MoS_2 given its lower ratio.

It is clear from the experimental observation that VS_2 exhibits better wetting characteristics when grown on mica than when grown on SiO_2. The mica(001) substrate is commonly believed to be a van der Waals-type layered material having a weak interaction with the overlayer grown on top of it. The van der Waals interaction is based on a purely physical Coulomb force through dipole interactions between the dipole moments from ionic or molecular species with the overlayer.[42] In other words, there is no transfer or sharing of electrons between ions or molecules. However, recent first-principle calculations of CdTe(111) on mica(001) reveal the van der Waals interaction only contributes to 20% of the total interfacial energy, the remaining 80% coming from chemical interaction with charge transfer between mica and the overlayer.[43] This may explain the epitaxial quality of the film on mica compared to the films grown on pure van der Waals surfaces such as graphene.[44] In the case of VS_2 on mica, it is likely that chemical interactions may also be involved to produce the high quality of the epitaxial superlattice VS_2 films (to be presented later) with a smoother morphology. For VS_2 on SiO_2, the wetting is not as complete as that on the mica surface. In the literature, flakes on SiO_2 standing at various angles have been reported in the growth of other 2D/3D heterostructures such as HfS_2/SiO_2[45] and SnS_2/SiO_2.[46] The fact that more tilted VS_2 flakes are observed on SiO_2 than on mica implies dangling-bond-assisted self-seeding growth occurs in some areas on the amorphous SiO_2 substrate.

One observation is noticed: the area immediately surrounding each large flake has fewer small flakes than observed in other areas as shown in Figure 2a, meaning the growth of the large flakes occurs at the expense of the smaller ones. This implies the diffusion length of small flakes (nuclei) is in the micrometer range at the optimized growth temperature. Overall, the frequent observation of flakes with lateral dimensions of over 100 μm in either case makes them the largest reported in the literature, whether by CVD[30,31] or hydrothermal methods.[47−49]

A diverse set of X-ray diffraction (XRD) scans was utilized to resolve the crystal structure of the APCVD-synthesized VS_2 flakes. θ–2θ scans of VS_2/mica were collected over a large range of 2θ. The pattern (not shown here) contains strong mica (00l) peaks (l = 2, 4, and 6), indicating its good single crystallinity with (001) orientation was well preserved after the high-temperature CVD growth process. One additional peak which cannot be attributed to mica is observed at about 15.64° (Figure 3a) and gives a d-spacing of ~5.661 ± 0.001 Å. This is assigned to VS_2 and is within 1.6% of the bulk VS_2 (1T phase, space group $P\bar{3}m1$, No. 164) d(001) spacing of 5.755 Å. This same peak is observed in VS_2 grown on amorphous SiO_2, in which a grazing incidence XRD (GIXRD) (Figure 3c) shows a sharp peak at 2θ = 15.653 ± 0.001° with a full width at half-maximum (fwhm, β) of 0.089 ± 0.001°, giving a d-spacing of about 5.657 ± 0.001 Å, 1.7% lower than the theoretical VS_2(001) value. The calculated average vertical coherent size extracted from the Bragg peak using the Scherrer formula[50] ($D \sim \lambda/(\beta \cos \theta)$, where λ is the X-ray wavelength, β is the peak's FWHM, and θ in units of radians is half the peak's 2θ location) is ~59 nm for VS_2/mica, slightly smaller than calculated for VS_2/SiO_2. This is consistent with the AFM thickness histograms plotted in Figure S2b,d, suggesting a narrower spread of flake thicknesses as well as smaller average thickness in VS_2 grown on mica as compared to those grown on SiO_2. In addition, the identified individual VS_2 peak implies the out-of-plane orientation is (001) on mica, whereas several weaker peaks are seen on SiO_2 from planes such as (100), (110), and (012) originating from flakes inclined at various angles. This is in good agreement with the optical microscopy observations of flat-lying flakes.

To measure the VS_2 nanoflakes' out-of-plane dispersions, rocking curves (RCs) were collected by fixing the X-ray source and detector on the VS_2(001) 2θ peak and rocking the sample about the horizontal axis perpendicular to the beam. The RC

DOI: 10.1021/acsanm.9b00608
ACS Appl. Nano Mater. 2019, 2, 3684−3694

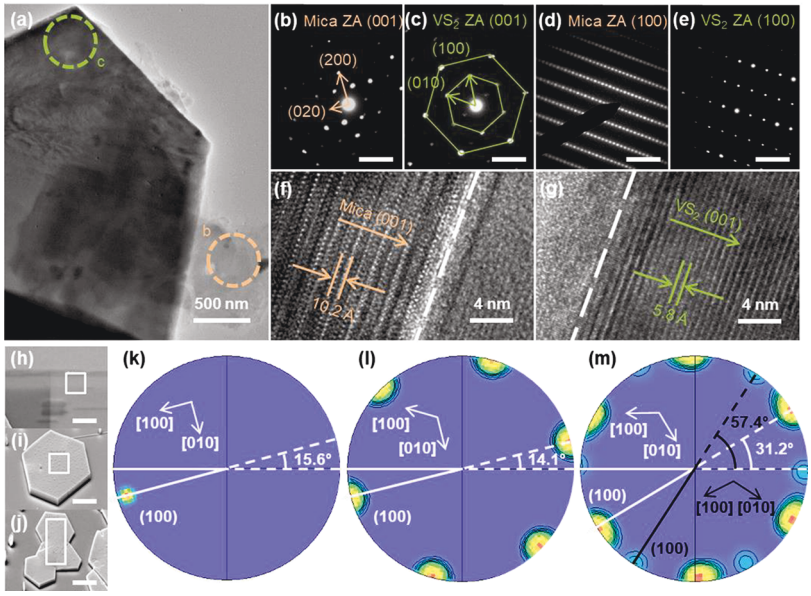

Figure 4. TEM analysis of VS_2 flakes grown on mica. (a) Low-magnification image showing individual VS_2 flake and exfoliated mica. (b, c) Plan-view SAED patterns from regions indicated in (a). Each indicates the (001) zone axis. (d, e) Cross-section SAED patterns from mica and VS_2, respectively. Each indicates the (100) zone axes. Scale bars on all SAED patterns are 4 nm^{-1}. (f, g) High-resolution TEM images of the VS_2/mica interface aligned to the mica (001) and VS_2(001) zone axes, respectively. SEM images of (h) bare mica, (i) individual VS_2 flake, and (j) merged VS_2 flakes. Scale bars are 10 μm. (k–m) (100) EBSD pole figures from the boxed regions in (h–j), respectively.

presents a single, reasonably sharp peak with a FWHM of 0.68 ± 0.01° for VS_2/mica (Figure 3b) but a nearly flat intensity profile for VS_2/SiO_2 (Figure 3d), again in agreement with the observed morphologies. Interestingly, this XRD characterization provides the additional information about intercalation-induced superstructure geometry over the stacking VS_2 frames as well. The slightly reduced lattice constant, c determined from flakes on both mica and SiO_2 substrates is consistent with V-rich VS_2,[30,51] where interstitial V atoms or clusters may be accommodated within the gaps of S–V–S trilayers at atmospheric pressure. Figures 3f and 3g show spatially resolved energy dispersive spectroscopy (EDS) maps of V Kα and S Kα signals, respectively, from the flake shown in Figure 3e. Each elemental signal is primarily confined to the flake. The noise in the surrounding clean substrate as well as the relatively low contrast is due to the flake's thin, sub-10 nm thickness. The V:S ratio is about 1.21 to 2, indicating a V-rich stoichiometry in this single VS_2 flake and supporting the decreased S–V–S trilayer spacing determined by XRD, which has been reported elsewhere. For instance, TEM intensity profiles presented by Ji et al.[30] show that V intercalation occurs without obvious structural distortion of the VS_2 framework. Furthermore, X-ray diffraction work by Poddar et al.[51] shows c in non-stoichiometric $V_{1.18}S_2$ is reduced from the bulk value, 5.75 Å, to 5.67 Å, consistent with our observation. Similar to the intercalation of organic and metal molecules,[52,53] there is a charge transfer between the VS_2 and the intercalated V that changes the original band structure of VS_2 and the charge density distribution in the V–VS_2 compound. This can affect the van der Waals interaction between VS_2 layers and thus the van der Waals gap distance. A detailed density function theory calculation specific to the charge transfer (electron donor or acceptor) and charge density distribution of the intercalated V in VS_2 is necessary to comment further on the nature of the decreased trilayer spacing in this system. This ratio has also been shown not to be sensitive to extended atmospheric exposure, suggesting negligible oxidation.

The phase and composition of the ultrathin VS_2 flakes were further investigated using room-temperature Raman spectroscopy as shown in Figure 3i. It can be seen that the Raman spectrum of an ultrathin VS_2 flake grown on SiO_2 shows the characteristic E_g (S in-plane) and A_g (S out-of-plane) peaks at ~263 and ~379 cm^{-1} with FWHM's of ~8 and ~12 cm^{-1}, respectively. As shown in Figure S6, the peaks' intensities increase with increasing VS_2 thickness. Previous study and our own experimental experiences have demonstrated that such VS_2 flakes are sensitive to the laser intensity and may decompose or react with oxygen if the characterization is conducted in atmosphere.[31] Consequently, multiple sets of Raman signals appear, which should not belong to VS_2. Herein, a vacuum optical stat was applied for our Raman characterization (see the Methods section for details). The obtained signals corresponding to the two vibrational modes of VS_2 match closely with the theoretical Raman peak locations of the bulk VS_2 structure (259.3 and 376.0 cm^{-1}; see the Supporting Information for calculation details). A compilation of Raman spectroscopy data from several sources is shown in Table S1. Of the current literature reports presenting Raman spectra of VS_2, only ours agrees with theoretical computation. Because Raman spectroscopy is a surface-sensitive characterization method, such observation over entire single flakes on the SiO_2 substrate illustrates the uniform VS_2 phase.

The combination of structural information provided by XRD scans and Raman spectra confirm that despite the V-rich stoichiometry observed via EDS, our synthesized nanoflakes exhibit a crystal structure consistent with VS_2 rather than monoclinic V_5S_8 (V:S = 1.25:2).[54] Although V_5S_8 is a commonly observed phase in the synthesis of vanadium–sulfur compounds,[30,55] these data indicate additional V atoms are intercalated between VS_2 layers without long-range structural order.

DOI: 10.1021/acsanm.9b00608
ACS Appl. Nano Mater. 2019, 2, 3684–3694

The aforementioned exploration of substrate effect has shown the disparate VS_2 growth behaviors to be due to the surface energy differences between mica and SiO_2. Compared to the VS_2 flakes grown on amorphous SiO_2 with uncertain in-plane and out-of-plane orientations, the flat-lying behavior of most flakes on mica is meaningful for further study. It has been reported that strain-free layered materials can be epitaxially grown on van der Waals substrates.[33] To determine the possible VS_2/mica epitaxial relationship, VS_2 flakes were initially transferred to a TEM grid by exfoliating from direct contact. Figure 4a shows a low-magnification plan-view TEM image of one VS_2 flake. Some of the underlying mica substrate exfoliated along with the flake can be seen protruding in the lower right corner of the image. Selected area electron diffraction (SAED) patterns were taken independently from regions b and c as shown by the dashed circles (Figure 4a), where the nonprimitive rectangular mesh in Figure 4b is consistent with mica pattern viewed from (001) and the hexagonal symmetry pattern (Figure 4c) consistent with (001) zone axis of 1T-VS_2.[31] This confirms the out-of-plane relation $VS_2(001)$||mica(001). Furthermore, from examining these plan-view diffraction patterns, we can determine the angle between $VS_2(100)$ and mica (100) to be ~4° for this flake. Note since $VS_2(100)$ plane is not parallel to $VS_2[100]$ direction, this is equivalent to ~34° between the $VS_2[100]$ and mica [100] directions. Figures 4f and 4g are high-resolution cross-section TEM images of the VS_2/mica interface. Two images were required rather than one because the mica and VS_2 in-plane zone axes did not perfectly align. When aligned to the proper zone axis, each material shows clear atomic periodicity, indicative of high-quality crystallization. Interlayer spacings of about 10.2 and 5.8 Å were measured for mica and VS_2, shown in Figures 4f and 4g, respectively, consistent with (001) out-of-plane for each (10.2 Å ~ $^1/_2c$ spacing of mica due to lack of symmetry between layers). SAED patterns collected on each side of the interface show the corresponding (100) zone axis for both mica and VS_2 (Figures 4d and 4e). Based on the tilted angles from one zone axis to the other, the relative angles (ϕ_{off}) between the $VS_2[100]$ and mica [100] are calculated (see the Supporting Information for details).

Electron backscatter diffraction (EBSD) pole figure analysis is another effective method to reveal the crystal orientation and potentially identify a preferred in-plane epitaxial relationship of VS_2 on mica. (001) pole figures of mica and individual VS_2 flakes (not shown here) showed single poles at the centers, indicative of (001) out-of-plane and in agreement with the TEM and XRD results. The uniform color across entire VS_2 flakes in inverse pole figures reveals the single crystal nature of these flakes. Further (100) EBSD pole figures corresponding to bare mica, a single VS_2 flake, and two conjoined VS_2 flakes are shown in Figure 4k–m. For single crystal mica with (001) out-of-plane, we expect to see one (100) pole at $\chi \sim 84.2°$ due to the low symmetry of the monoclinic unit cell. Experimentally, Figure 4k shows one pole at $\chi \sim 84.6°$ and about 15.6° below horizontal. The inferred unit axes' directions are superimposed on the data. Single-crystal $VS_2(001)$ theoretically should exhibit six poles $\{(0\bar{1}0), (010), (\bar{1}00), (100), (\bar{1}10),$ and $(1\bar{1}0)\}$ spaced 60° azimuthally at angle $\chi = 90°$. Figure 4l,m confirms six {100} poles from each VS_2 flake; thus, each flake is single crystalline. The pole figure in Figure 4m exhibits two sets of poles due to signal from two flakes which merged during growth. Nevertheless, the corresponding unit axes can be identified. The comparison of (100) pole figures from mica and VS_2 flake gives the angles, denoted ϕ_{off}, between $VS_2[100]$ and mica [100] with values of 31.5°, 14.4°, and 11.8° (±1°) for three flakes.

A geometrical superlattice area mismatching (GSAM) model based on the minimization of superlattice area mismatch was used to calculate possible interface lattice arrangements between VS_2 and mica.[56,57] Although typically used for conventional 3D/3D heterostructures, its recent application to a vdW heterostructure has also been successful.[25,58] The most likely superlattice results are tabulated in Table S2, with the relative rotation angle, ϕ_{off}, defined as the angle between $VS_2[100]$ and mica [100]. Figure S4a shows the corresponding bubble plot of ΔA vs ϕ_{off}. The bubbles' radii have been scaled inversely proportional to A (larger bubbles correspond to smaller superlattice areas). The superlattice area A is defined as the area in which a near coincident lattice occurs between the overlayer and the substrate. Superlattice area mismatch, ΔA, is defined as the area over which the film and substrate superlattices do not overlap. Considering the 6-fold rotational symmetry of the VS_2 unit mesh, only results from 0° to 60° are plotted. Figure S4b shows schematics of the S-terminated unit mesh of $VS_2(001)$, the K-terminated unit mesh of mica(001), and the smallest calculated superlattice (ϕ_{off} = 30.0°). This geometrical superlattice area mismatching simulation corresponds well to the angle values determined from TEM, EBSD pole figure analysis, and the statistical measurement over 120 triangular VS_2 flakes on mica from optical microscopy images (Figure S4c).

A histogram of all 130 observed ϕ_{off} values is superimposed on the superlattice area matching calculation results in Figure S4a. The most frequently observed ϕ_{off} angles coincide with those predicted by the calculation. In fact, the greatest number of flakes are observed at ϕ_{off} = 30°, in agreement with the most likely superlattice. Despite the inconclusive results from XRD azimuthal phi scans due to lack of intensity, a combination of TEM diffraction patterns, EBSD pole figures, and optical microscopy sampling show strong agreement with the simulation. This clear accordance between calculation and experiment is remarkable considering the weak van der Waals interaction between mica and VS_2, each of which exhibits a layered structure. Recent first-principles calculations of interfacial energies including both the chemical and the nonlocal vdW interactions between a soft layered perovskite $CsPbBr_3$ film and mica substrate[59] as well as a 3D CdTe film on mica[43] indicate that an additional chemical interaction can play a role in the formation of the interface. In our case, besides the van der Waals interaction, we cannot rule out the possibility of the existence of an additional chemical interaction at the film mica interface to enhance the nucleation and growth of the VS_2 crystals.

Recent density functional theory (DFT) calculations have predicted VS_2 to be a promising next-generation 2D magnet by demonstrating the extraordinary metallic property and intrinsic ferromagnetism in the ultrathin to monolayer VS_2.[13−20] Experimentally, the electrical properties of VS_2 flakes were studied by room temperature current−voltage (I−V) measurements using a two-point-probe system in an SEM (see the Supporting Information for details). The average resistivity of one ~13 nm thick VS_2 flake as-grown on a silicon substrate was measured to be 1.8 ± 0.1 μΩ·m, which indicates a metallic nature and is comparable to others' results.[30,31] In addition, magnetic force microscopy (MFM) is an inherently localized

DOI: 10.1021/acsanm.9b00608
ACS Appl. Nano Mater. 2019, 2, 3684−3694

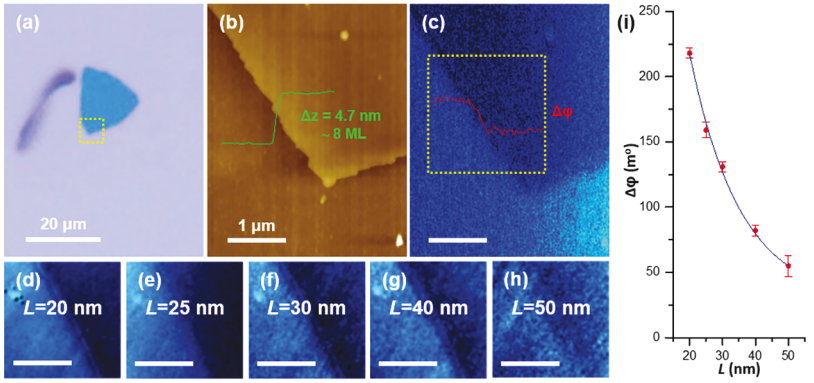

Figure 5. (a) Optical image of ultrathin VS_2 flake on SiO_2 substrate. (b) AFM topography scan revealing flake thickness to be about 4.7 nm thick, corresponding to eight S−V−S trilayers. (c) MFM phase map of area shown in (b), collected at a lift height of 25 nm. (d−h) MFM phase maps of VS_2/SiO_2 interface at lift heights, L = 20, 25, 30, 40, and 50 nm. Scale bars in (b−h) are 1 μm. (i) MFM phase contrast of ultrathin flake measured at several lift heights between 20 and 50 nm. An exponential fit is included to guide the eye.

characterization technique and has optical microscopy capabilities for easy identification of regions of interest, making it ideal for studying the magnetic properties of nanomaterials. The MFM data collection begins with a traditional noncontact AFM scan to map the sample's topography by measuring the attractive van der Waals forces between the sample and the probe tip. After topography data were acquired, the tip is lifted a preset distance (typically 20−50 nm) beyond the influence of the vdW forces. It then follows the collected topography line scan to maintain a constant sample−probe distance and detects magnetic interactions via a shift in the cantilever's vibrational phase.

Figure 5 shows an optical image along with AFM topography and MFM phase maps of an ∼4.7 nm thick VS_2 flake on SiO_2. In Figure 5a, the optical image shows an ultrathin flake with a diameter of about 20 μm that is visible due to optical interference with the 300 nm SiO_2/Si substrate. Figure 5b shows an AFM topography map of the dashed box area in Figure 5a, which demonstrates the thickness of the flake to be about 4.7 nm, corresponding to eight S−V−S layers. An MFM phase map collected at a lift height of 25 nm is shown in Figure 5c. The negative phase shift of the sample relative to the SiO_2 substrate, which is weakly diamagnetic (essentially nonmagnetic), indicates an attraction between the VS_2 flake and the MFM cantilever. This phase contrast was not observed when the sample and tip were unmagnetized. Furthermore, because one phase contrast was measured across the entirety of each flake, one can infer that each flake is composed of just one magnetic domain.

To demonstrate the dependence of MFM phase contrast on sample−tip distance, data were collected at lift heights (L) of 20, 25, 30, 40, and 50 nm (shown in Figure 5d−h). Qualitatively, one observes a decrease in the interfacial contrast with an increase in L. Averaging over ∼50 line scans across the flake/substrate interface ensures the data's reliability and provides optimal signal-to-noise. Quantitative results are plotted in Figure 5i. The exponential decay of MFM phase shift with an increase in lift height likewise indicates an exponential decrease in attractive force between the tip and sample, consistent with what one would expect for a magnetic interaction.[60−62] The observation of magnetic force microscopy phase signal provides evidence for the existence of ferromagnetism in ultrathin VS_2, consistent with density functional theory calculations.[19] This negative MFM phase shift was reproducibly measured for several flakes ranging in thickness from 5 to 20 nm with consistent results. In fact, slightly stronger phase signal (indicating stronger magnetization) was measured as thickness decreased, consistent with theoretical predictions.[19]

It is worth commenting on the effects of oxidation which occurs on the surfaces of most metals when exposed to atmosphere. In many metals (e.g., Co, Cu, and V) surface oxidation is self-limiting, extending down into only the top several atomic layers. This metal oxide then serves as a passivation layer which protects the bulk metal from oxidation. Assuming our VS_2 nanoflake samples form self-limiting oxides at the surface, MFM measurements are detecting signal from a thinner region than directly reported by AFM. For instance, the 4.7 nm thickness (8 ML) measured for the flake shown in Figure 5a may actually be a measurement of the total thickness of VS_2 + VS oxide. The measured magnetic signal is thus from an even thinner film of VS_2, which is capped by a protective oxide. Future experiments may be conducted to determine the extent to which VS_2 is oxidized in atmosphere and the level to which it contributes to magnetic measurements. In addition, magnetic measurements may be conducted *in situ*, or samples may be capped with a thin layer of a nonoxidizing material prior to atmospheric exposure to prevent surface oxide formation.[28] These preliminary findings should be expanded upon by future experiments using other methods such as MOKE microscopy and SQUID magnetometry which would provide definitive proof of a ferromagnetic signal.[4,9]

CONCLUSION

An APCVD method has been utilized to successfully grow large, ultrathin and high-quality vanadium disulfide crystals on amorphous SiO_2 and single crystal muscovite mica(001) substrates. By varying several of the many synthesis parameters, we have achieved flakes with the largest lateral dimensions of those reported in the literature. The surface on which V and S adatoms nucleate was shown to impact the nanoflakes' lateral size, thickness, and morphology. Flakes grown on mica exhibit a higher tendency of lying flat as compared to those grown on SiO_2. Data from a combination of several characterization techniques provide evidence for in-plane epitaxy formation between VS_2 and mica, which agrees with a geometrical superlattice area mismatch model typically used for heterostructures. Electrical current−voltage measure-

DOI: 10.1021/acsanm.9b00608
ACS Appl. Nano Mater. 2019, 2, 3684−3694

ments confirm the metallic nature of the flakes, while magnetic force microscopy measurements were used to observe ferromagnetism in ultrathin flakes at room temperature. This serves as the first report of measurable magnetic signal from ultrathin VS_2 collected by MFM, which may be expanded upon for quantification of ferromagnetic properties. In addition to their current applications in electrodes,[30] batteries,[49] hydrogen evolution reaction,[31,47] supercapacitors,[48,63] and moisture sensors,[64] ultrathin VS_2 nanoflakes show promise for implementation in spintronic circuits and quantum computing devices.

METHODS

Growth of Large Ultrathin VS_2 Flakes on Mica and SiO_2/Si(100) by APCVD. The APCVD setup is shown in Figure 1a. The furnace has two temperature zones: one for heating the S precursor boat and one for heating the VCl_3 precursor boat and the substrates. The quartz tube (Technical Glass Products, Painesville, OH) has an inner diameter of 1.6 cm and a length of 101.6 cm and was mounted within an insulating alumina tube (AdValue Technology, Tucson, AZ) with a 25.4 mm inner diameter and 1219 mm in length. The mica substrates (SPI Chem Mica grade V-4, 25 × 75 × 0.26 mm^3) were cut and cleaved into smaller and thinner pieces, which were about 13 × 75 × 0.08 mm^3. The Si substrates with 300 nm oxide layer (Silicon Quest International, San Jose, CA) were measured to be about 13 × 75 × 0.5 mm^3. Several substrates were placed downstream from the VCl_3 source boat facing upward, while an additional substrate was placed on top of the VCl_3 source boat facing downward. Six growth parameters including S precursor amount, VCl_3 precursor amount, carrier gas type, carrier gas flow rate, heating zone temperatures, and growth duration were varied systematically to obtain the largest ultrathin VS_2 flakes. In the optimized growth conditions, a quartz boat containing 0.1 g of VCl_3 (Sigma-Aldrich) was placed in the center of zone I, and a quartz boat containing 0.6 g of S (Sigma-Aldrich) was positioned in the center of zone II, 25 cm upstream. Both boats were semicylindrical cuts from a quartz tube of 1.5 cm outer diameter. Having no vertical edges perpendicular to the direction of gas flow allows for uniform transport of the precursor materials to the substrates. The growth procedure is illustrated in Figure 1b. Before the growth, the quartz tube was loaded with the precursors and substrates and baked at ∼120 °C (zone I) while purging with 80 sccm forming gas (3% H_2 balanced in N_2) for 1 h. Then, with the gas flow held at 80 sccm, zone I was heated from 120 to ∼750 °C at a rate of ∼80 °C/min. Simultaneously, zone II was heated from 45 °C (due to radiative heat from zone I) to 250 °C at a rate of ∼32 °C/min. Once the temperatures of zones I and II reached 750 and 250 °C, respectively, the gas flow rate was reduced to 50 sccm. After the 10 min growth of VS_2 under the atmospheric pressure, the flow rate was increased to 80 sccm, and the heaters were turned off. The system naturally cooled to room temperature over ∼2.5 h. The as-grown samples were first characterized by optical imaging, and the substrate placed on top of the VCl_3 boat gave the best growth results. These samples were examined further by using various techniques.

Note that metal halides such as VCl_3 are hydroscopic. The use of a hydroscopic precursor increases the partial pressure within the furnace as the temperature increases.[65] Thus, we stored VCl_3 in an Ar glovebox and retrieved the needed amount immediately before each synthesis to reduce exposure to moisture. We have used either pure Ar or forming gas as the carrier gas for synthesis. We found the VS_2 flakes grown using forming gas are larger than those grown using pure Ar. We believe the hydrogen from the forming gas plays a crucial role in the chemical reaction. The H_2 reduces S_2 to S_2^{4-} while the Cl remains in the Cl^- state, combining with the H^+ cation to form HCl, which is then carried away by the flowing gas. An additional advantage of forming gas is that the thermal conductivity of hydrogen is about 1 order of magnitude higher than that of Ar (∼0.23 W/(m K) vs ∼0.022 W/(m K) at 400 K). Thus, hydrogen molecules aid in heat transfer from the furnace to the precursors and substrates, enhancing the energy available for chemical reactions.

Characterization Methods. *Imaging.* Optical images were taken on a Nikon Eclipse Ti-S inverted optical microscope. AFM images were taken using a Park Systems XE100 scanning probe microscope in noncontact mode at a selected frequency ∼190 kHz using a cantilever with a spring constant of ∼45 N m^{-1}. SEM (Carl Zeiss Supra 55 field emission) images were collected at 5 keV with a 30 μm aperture, while 10 keV was used for EDS measurements.

X-ray Diffraction (XRD) and X-ray Pole Figure. XRD scans were obtained using a Bruker D8 Discover X-ray diffractometer with a Cu source (Cu Kα, λ = 1.5405 Å, 40 kV, 40 mA) and a point detector. The incident beam, detector, and antiscatter slits used to achieve maximum resolution were 0.1, 0.1, and 0.2 mm, respectively. The 0.6 mm slits were used for azimuthal scans to enhance intensity. The step sizes used for θ–2θ, rocking curve (RC), and azimuthal ϕ scans are 0.001°, 0.001°, and 0.1°, respectively.

Transmission Electron Microscopy (TEM). The VS_2 sample used in TEM was protected by a Pt coating and thinned by focused ion beam milling using energetic Ga^+ ions and the *in situ* specimen lift-out technique. The thinned sample was mounted on a liquid nitrogen cooled sample stage to minimize mechanical drifting of the sample. A 200 keV electron beam was used to obtain the TEM (JEOL 2100 F) bright-field images, high-resolution images, and electron diffraction patterns. Atomic percentages converted from the weight percentages of the elements in VS_2 flake, at the interface of mica and VS_2, and mica were collected by EDS in the same system (Figure S5).

Electron Backscatter Diffraction (EBSD) and Energy Dispersive Spectroscopy (EDS). EBSD characterizations of VS_2 flakes on mica were performed with a Carl Zeiss Ultra 1540 EsB SEM-FIB system integrated with a NordlysNano EBSD Detector (Oxford Instruments). To avoid electrical charging from the mica substrate, the sample was sputtered with a several nanometers thick Pt film before the EBSD scan. A 15 kV electron beam in high current mode with a 120 μm aperture was used to scan the sample surface to locate a flake. The EBSD scanning was conducted on the flake surface in a 5.0 × 5.0 μm^2 area with a step size of 125 nm. The scans were acquired at a working distance of 18 mm and 70° sample tilt. The crystallographic orientation data were collected by using Aztec 2.1 EBSD data acquisition software and postanalyzed using the HKL Channel 5 Tango and Mambo software package (Oxford Instruments) for the crystallographic orientation mapping, the grain boundary misorientation estimation, and the pole figure plotting. EDS spectra were also collected simultaneously using an X-Max silicon drift detector (Oxford Instrument) in the SEM-FIB system under the same working configurations.

Raman Spectroscopy. Raman spectra were collected using cryo-Raman measurements with a homemade micro-Raman spectrometer. To achieve an isolated environment and prevent the possible oxidation of vanadium disulfide caused by laser irradiation in atmosphere, the sample was mounted in an optical cryostat with a quartz window. Before measurement, the internal pressure of the cryostat was pumped down to ∼7 × 10^{-7} Torr by a Turbo pump (HiCube 80 Eco, Pfeiffer Vacuum, Germany). For room temperature measurements, the cryostat was pumped down without filling the cavity with liquid nitrogen. The 532 nm laser with a spot size of 2 μm and 1 mW intensity (LRS-0532 DPSS, Laserglow Technologies, Canada) was irradiated via a 50× objective lens. The reflected signal was obtained and analyzed by a high-speed spectroscopy CCD camera (iDus 420 Series, Andor Technology Ltd., UK) and imaging spectrometer (Shamrock 500i, Andor Technology Ltd., UK). The resolution of the Raman system was 0.6 cm^{-1}. The step size used in measurements was 1.34 cm^{-1}. All spectra were collected by integrating the signal for 120 s. The Raman shifts ranging from 220 to 420 cm^{-1} were investigated in each measurement (Figure S6).

Electrical Measurement. Electrical measurements were collected with the sample mounted in a Carl Zeiss Ultra 1540 EsB SEM-FIB system. Two tungsten probes (Signatone SM-10) were positioned by adjusting micrometers to make contacts with the selected flake. A Keithley (4200-SCS) source meter in sweep current mode was used

DOI: 10.1021/acsanm.9b00608
ACS Appl. Nano Mater. 2019, 2, 3684−3694

to measure the $I-V$ data. The current was swept from −5 to +5 μA in either 0.05 or 0.01 μA increments to give 201 or 1001 data points, respectively. In addition, room-temperature resistivity of one ultrathin VS_2 flake was measured using a prototype of Xallent's Nanoprober A100 at Cornell's NanoScale Science and Technology Facility. In this setup, a prearranged linear four-point probe made of Pt with ∼300 nm probe widths and ∼700 nm probe separation was pressed on top of the flake to make electrical contact. The resistance values were collected from two different locations with multiple measurements (three measurements for the first location and four measurements for the second location). Results are included in the Supporting Information.

MFM Measurements. A Park Systems NX20 scanning probe microscope with a Park MFMR cantilever ($k \sim 2.8$ N m^{-1}, selected frequency ∼75 kHz, CoCr coated with nominal coercivity ∼400 Oe) was used for MFM measurements. Both the sample and tip were magnetized by an ∼500 Oe permanent magnet prior to collection. The measurement was conducted in the conventional two-pass method (first in noncontact AFM mode for topographic contrast, second at a preset lift height for magnetic contrast).

Theoretical Calculation Methods. *First-Principles Calculation of the Surface Energy of VS_2.* The surface energy of different crystal planes of the VS_2 was studied by the first-principles. The calculations were based on density function theory where the local density approximation was chosen to describe the exchange and correlation energies of electrons. A 2 × 2 × 2 supercell of VS_2 with an energy cutoff of 310 eV and a Monkhorst−Pack k-point grid 5 × 5 × 1 was used. The interaction between core electrons and valence electrons was treated by means of ultrasoft pseudopotentials (see details in the Supporting Information).

Density Functional Theory Calculation of Raman Peaks. Within the density functional theory local density approximation, the norm-conserving pseudopotentials were used to mimic the scattering behaviors of the V and S atoms. We used a plane-wave basis whose expansion was cut off at E_{cut} = 1224.51 eV and a 4 × 4 × 4 Monkhorst−Pack grid sampling of the first Brillouin zone. The calculations were considered convergent when the energy difference between self-consistent iteration was smaller than 1.3606×10^{-5} eV. The ground state was obtained by relaxing the geometry and the atomic coordinates. The atoms in the system were considered in equilibrium when the force on each individual atom was smaller than 0.0025 eV/Å.

Geometrical Superlattice Area Mismatching. Defining u_1 and v_1 (u_2 and v_2) as the substrate (overlayer) superlattice lengths separated by angle α_1 (α_2), there are two criteria for determining the relative likelihood of observing a calculated superlattice: (i) the substrate superlattice area, A_1, and overlayer superlattice area, A_2, should be small to increase the density of coincident atomic sites; (ii) the difference between the two superlattice areas, ΔA, should be small to minimize the interfacial energy of the heteroepitaxial system. ΔA is defined as

$$\Delta A = A(\Delta u/u + \Delta v/v + \Delta\alpha/\tan\alpha) \quad (2)$$

where Δu, Δv, and $\Delta\alpha$ are the differences in each parameter between the substrate and overlayer. Smallest values of A and ΔA represent the highest chance of observing a given superlattice.

The surface termination of freshly cleaved mica(001) has been examined by others via Auger electron spectroscopy[66] and shows about half a monolayer (ML) of potassium (K). The substrate lattice parameters used in the superlattice area mismatch model are those of the K-terminated mica (001) surface: a_{mica} = 5.192 Å, b_{mica} = 5.189 Å, and α_{mica} = 60.02°. The overlayer lattice parameters used are those of VS_2(001): a_{VS_2} = 3.221 Å, b_{VS_2} = 3.221 Å, and α_{VS_2} = 120°. The calculation was conducted with A constrained to <300 Å^2 and $\Delta u/u$, $\Delta v/v$, and $\Delta\alpha/\tan\alpha$ each set to <8%.

■ ASSOCIATED CONTENT

Supporting Information

The Supporting Information is available free of charge on the ACS Publications website at DOI: 10.1021/acsanm.9b00608.

Additional AFM scans of VS_2 flakes; lateral size and thickness histograms of VS_2 flakes grown on SiO_2 and mica substrates; geometrical superlattice area matching results of VS_2/mica; VS_2 Raman spectroscopy data from several references; first-principles calculation of VS_2 surface energy; angle determination of VS_2[100] and mica[100] from TEM results; VS_2 electrical current−voltage measurement; cross-section TEM EDS data; Raman spectra of VS_2 flakes of increasing thicknesses (PDF)

■ AUTHOR INFORMATION

Corresponding Author

*E-mail aaron_littlejohn@yahoo.com.

ORCID

Aaron J. Littlejohn: 0000-0002-7082-5601
Zonghuan Lu: 0000-0003-2375-8247
Xin Sun: 0000-0001-5633-3371
Yiping Wang: 0000-0001-7626-3278
Sufei Shi: 0000-0001-5158-805X
Jian Shi: 0000-0003-2115-2225
Humberto Terrones: 0000-0003-0515-0721
Kim M. Lewis: 0000-0002-8342-8699

Author Contributions

A.J.L. and Z.L. contributed equally. A.J.L. and Z.L. initiated and performed the project with supervision from M.W., T.-M.L. and G.-C.W. Z.H.L. collected electron backscatter diffraction data. X.S., Y.L., T.W., Y.H., and S.-F.S. provided facilities for and aided in the collection of Raman spectra. A.R. and H.T. calculated the theoretical Raman modes of 1T-VS_2. Y.W. and J.S. conducted preliminary TEM characterization and provided optical microscopy facilities. L.H.Z. and K.K. collected high-resolution transmission electron microscopy. P.N. and K.M.L. conducted electrical current−voltage measurements. W.S. aided in the collection of magnetic force microscopy data. H.L. conducted surface energy calculations. A.J.L. and Z.L. wrote the manuscript with input from all coauthors.

Notes

The authors declare no competing financial interest.

■ ACKNOWLEDGMENTS

This work was supported by the New York State's Empire State Development's Division of Science, Technology and Innovation (NYSTAR) through Focus Center Contract C150117, the National Science Foundation CMMI 1635520, Royal Thai Government Scholarship (P.N.), Rensselaer's Micro and Nano Fabrication Clean Room, and Rensselaer. H.T. and A.R. are grateful to the National Science Foundation (EFRI-1433311). The supercomputer time was provided by the Center for Computational Innovations (CCI) at Rensselaer Polytechnic Institute and the Extreme Science and Engineering Discovery Environment (XSEDE, Project TG-DMR17008), which was supported by National Science Foundation Grant ACI-1053575. TEM and EDS studies were performed in whole at Center for Functional Nanomaterials,

DOI: 10.1021/acsanm.9b00608
ACS Appl. Nano Mater. 2019, 2, 3684−3694

BNL, operated by the U.S. DOE, Office of Basic Sciences under Contract DE-SC001270T.4. AFM and MFM images were acquired using a Park NX20 SPM system. T.W. and S.-F.S. acknowledge support from AFOSR through Grant FA9550-18-1-0312.

REFERENCES

(1) Geim, A. K.; Grigorieva, I. V. Van der Waals heterostructures. *Nature* **2013**, *499*, 419−425.
(2) de Jongh, L. J. Experiments on simple magnetic model systems. *J. Appl. Phys.* **1978**, *49* (3), 1305−1310.
(3) Carteaux, V.; Moussa, F.; Spiesser, M. Ising-like ferromagnetic behaviour for the lamellar $Cr_2Si_2Te_6$ compound: a neutron scattering investigation. *EPL (Europhysics Letters)* **1995**, *29* (3), 251−256.
(4) Huang, B.; Clark, G.; Navarro-Moratalla, E.; Klein, D. R.; Cheng, R.; Seyler, K. L.; Zhong, D.; Schmidgall, E.; McGuire, M. A.; Cobden, D. H.; Yao, W.; Xiao, D.; Jarillo-Herrero, P.; Xu, X. Layer-dependent ferromagnetism in a van der Waals crystal down to the monolayer limit. *Nature* **2017**, *546* (7657), 270−273.
(5) Wang, X.; Du, K.; Fredrik Liu, Y. Y.; Hu, P.; Zhang, J.; Zhang, Q.; Owen, M. H. S.; Lu, X.; Gan, C. K.; Sengupta, P.; Kloc, C.; Xiong, Q. Raman spectroscopy of atomically thin two-dimensional magnetic iron phosphorus trisulfide ($FePS_3$) crystals. *2D Mater.* **2016**, *3* (3), 031009.
(6) Tian, Y.; Gray, M. J.; Ji, H.; Cava, R. J.; Burch, K. S. Magneto-elastic coupling in a potential ferromagnetic 2D atomic crystal. *2D Mater.* **2016**, *3* (2), 025035.
(7) Carteaux, V.; Brunet, D.; Ouvrard, G.; Andre, G. Crystallographic, magnetic and electronic structures of a new layered ferromagnetic compound $Cr_2Ge_2Te_6$. *J. Phys.: Condens. Matter* **1995**, *7* (1), 69−87.
(8) Mermin, N. D.; Wagner, H. Absence of Ferromagnetism or Antiferromagnetism in One- or Two-Dimensional Isotropic Heisenberg Models. *Phys. Rev. Lett.* **1966**, *17* (22), 1133−1136.
(9) Gong, C.; Li, L.; Li, Z.; Ji, H.; Stern, A.; Xia, Y.; Cao, T.; Bao, W.; Wang, C.; Wang, Y.; Qiu, Z. Q.; Cava, R. J.; Louie, S. G.; Xia, J.; Zhang, X. Discovery of intrinsic ferromagnetism in two-dimensional van der Waals crystals. *Nature* **2017**, *546* (7657), 265−269.
(10) Cai, L.; He, J.; Liu, Q.; Yao, T.; Chen, L.; Yan, W.; Hu, F.; Jiang, Y.; Zhao, Y.; Hu, T.; Sun, Z.; Wei, S. Vacancy-Induced Ferromagnetism of MoS_2 Nanosheets. *J. Am. Chem. Soc.* **2015**, *137* (7), 2622−2627.
(11) Wang, Y.; Tseng, L.-T.; Murmu, P. P.; Bao, N.; Kennedy, J.; Ionesc, M.; Ding, J.; Suzuki, K.; Li, S.; Yi, J. Defects engineering induced room temperature ferromagnetism in transition metal doped MoS_2. *Mater. Des.* **2017**, *121*, 77−84.
(12) Yan, S.; Qiao, W.; He, X.; Guo, X.; Xi, L.; Zhong, W.; Du, Y. Enhancement of magnetism by structural phase transition in MoS_2. *Appl. Phys. Lett.* **2015**, *106* (1), 012408.
(13) Jing, Y.; Zhou, Z.; Cabrera, C. R.; Chen, Z. Metallic VS_2 Monolayer: A Promising 2D Anode Material for Lithium Ion Batteries. *J. Phys. Chem. C* **2013**, *117* (48), 25409−25413.
(14) Ataca, C.; Şahin, H.; Ciraci, S. Stable, Single-Layer MX_2 Transition-Metal Oxides and Dichalcogenides in a Honeycomb-Like Structure. *J. Phys. Chem. C* **2012**, *116* (16), 8983−8999.
(15) Gao, D.; Xue, Q.; Mao, X.; Wang, W.; Xu, Q.; Xue, D. Ferromagnetism in ultrathin VS_2 nanosheets. *J. Mater. Chem. C* **2013**, *1* (37), 5909−5916.
(16) Rodgers, P. Let there be magnetism. *Nat. Nanotechnol.* **2012**, 03052012.
(17) Ma, Y.; Dai, Y.; Guo, M.; Niu, C.; Zhu, Y.; Huang, B. Evidence of the Existence of Magnetism in Pristine VX_2 Monolayers (X = S, Se) and Their Strain-Induced Tunable Magnetic Properties. *ACS Nano* **2012**, *6* (2), 1695−1701.
(18) Zhuang, H. L.; Hennig, R. G. Stability and magnetism of strongly correlated single-layer VS_2. *Phys. Rev. B: Condens. Matter Mater. Phys.* **2016**, *93* (5), 054429.
(19) Zhang, H.; Liu, L.-M.; Lau, W.-M. Dimension-dependent phase transition and magnetic properties of VS_2. *J. Mater. Chem. A* **2013**, *1* (36), 10821−10828.
(20) Zhou, Y.; Yang, C.; Xiang, X.; Zu, X. Remarkable magnetism and ferromagnetic coupling in semi-sulfuretted transition-metal dichalcogenides. *Phys. Chem. Chem. Phys.* **2013**, *15* (34), 14202−14209.
(21) Zhang, Y.; Wu, X. Vanadium sulfide nanoribbons: Electronic and magnetic properties. *Phys. Lett. A* **2013**, *377* (43), 3154−3157.
(22) Mulazzi, M.; Chainani, A.; Katayama, N.; Eguchi, R.; Matsunami, M.; Ohashi, H.; Senba, Y.; Nohara, M.; Uchida, M.; Takagi, H.; Shin, S. Absence of nesting in the charge-density-wave system1T-VS_2 as seen by photoelectron spectroscopy. *Phys. Rev. B: Condens. Matter Mater. Phys.* **2010**, *82* (7), 075130.
(23) Gauzzi, A.; Sellam, A.; Rousse, G.; Klein, Y.; Taverna, D.; Giura, P.; Calandra, M.; Loupias, G.; Gozzo, F.; Gilioli, E.; Bolzoni, F.; Allodi, G.; De Renzi, R.; Calestani, G. L.; Roy, P. Possible phase separation and weak localization in the absence of a charge-density wave in single-phase1T-VS_2. *Phys. Rev. B: Condens. Matter Mater. Phys.* **2014**, *89* (23), 235125.
(24) Zhong, M.; Li, Y.; Xia, Q.; Meng, X.; Wu, F.; Li, J. Ferromagnetism in VS_2 nanostructures: Nanoflowers versus ultrathin nanosheets. *Mater. Lett.* **2014**, *124*, 282−285.
(25) Guo, Y.; Deng, H.; Sun, X.; Li, X.; Zhao, J.; Wu, J.; Chu, W.; Zhang, S.; Pan, H.; Zheng, X.; Wu, X.; Jin, C.; Wu, C.; Xie, Y. Modulation of Metal and Insulator States in 2D Ferromagnetic VS_2 by van der Waals Interaction Engineering. *Adv. Mater.* **2017**, *29* (29), 1700715.
(26) Niu, J.; Yan, B.; Ji, Q.; Liu, Z.; Li, M.; Gao, P.; Zhang, Y.; Yu, D.; Wu, X. Anomalous Hall effect and magnetic orderings in nanothick V_5S_8. *Phys. Rev. B: Condens. Matter Mater. Phys.* **2017**, *96* (7), 075402.
(27) Hardy, W. J.; Yuan, J.; Guo, H.; Zhou, P.; Lou, J.; Natelson, D. Thickness-Dependent and Magnetic-Field-Driven Suppression of Antiferromagnetic Order in Thin V_5S_8 Single Crystals. *ACS Nano* **2016**, *10* (6), 5941−5946.
(28) Bonilla, M.; Kolekar, S.; Ma, Y.; Diaz, H. C.; Kalappattil, V.; Das, R.; Eggers, T.; Gutierrez, H. R.; Phan, M.-H.; Batzill, M. Strong room-temperature ferromagnetism in VSe_2 monolayers on van der Waals substrates. *Nat. Nanotechnol.* **2018**, *13* (4), 289−293.
(29) Arnold, F.; Stan, R.-M.; Mahatha, S. K.; Lund, H. E.; Curcio, D.; Dendzik, M.; Bana, H.; Travaglia, E.; Bignardi, L.; Lacovig, P.; Lizzit, D.; Li, Z.; Bianchi, M.; Miwa, J. A.; Bremholm, M.; Lizzit, S.; Hofmann, P.; Sanders, C. E. Novel single-layer vanadium sulphide phases. *2D Mater.* **2018**, *5* (4), 045009.
(30) Ji, Q.; Li, C.; Wang, J.; Niu, J.; Gong, Y.; Zhang, Z.; Fang, Q.; Zhang, Y.; Shi, J.; Liao, L.; Wu, X.; Gu, L.; Liu, Z.; Zhang, Y. Metallic Vanadium Disulfide Nanosheets as a Platform Material for Multifunctional Electrode Applications. *Nano Lett.* **2017**, *17* (8), 4908−4916.
(31) Yuan, J.; Wu, J.; Hardy, W. J.; Loya, P.; Lou, M.; Yang, Y.; Najmaei, S.; Jiang, M.; Qin, F.; Keyshar, K.; Ji, H.; Gao, W.; Bao, J.; Kono, J.; Natelson, D.; Ajayan, P. M.; Lou, J. Facile Synthesis of Single Crystal Vanadium Disulfide Nanosheets by Chemical Vapor Deposition for Efficient Hydrogen Evolution Reaction. *Adv. Mater.* **2015**, *27* (37), 5605−5609.
(32) Sun, X.; Lu, Z.; Xie, W.; Wang, Y.; Shi, J.; Zhang, S.; Washington, M. A.; Lu, T.-M. van der Waals epitaxy of CdS thin films on single-crystalline graphene. *Appl. Phys. Lett.* **2017**, *110* (15), 153104.
(33) Wang, Y.; Shi, Y.; Xin, G.; Lian, J.; Shi, J. Two-Dimensional van der Waals Epitaxy Kinetics in a Three-Dimensional Perovskite Halide. *Cryst. Growth Des.* **2015**, *15* (10), 4741−4749.
(34) Li, X.; Li, X.; Zang, X.; Zhu, M.; He, Y.; Wang, K.; Xie, D.; Zhu, H. Role of hydrogen in the chemical vapor deposition growth of MoS_2 atomic layers. *Nanoscale* **2015**, *7* (18), 8398−8404.
(35) McCreary, K. M.; Hanbicki, A. T.; Jernigan, G. G.; Culbertson, J. C.; Jonker, B. T. Synthesis of Large-Area WS_2 monolayers with Exceptional Photoluminescence. *Sci. Rep.* **2016**, *6* (1), 19159.

DOI: 10.1021/acsanm.9b00608
ACS Appl. Nano Mater. 2019, 2, 3684−3694

(36) Gong, Y.; Ye, G.; Lei, S.; Shi, G.; He, Y.; Lin, J.; Zhang, X.; Vajtai, R.; Pantelides, S. T.; Zhou, W.; Li, B.; Ajayan, P. M. Synthesis of Millimeter-Scale Transition Metal Dichalcogenides Single Crystals. *Adv. Funct. Mater.* **2016**, *26* (12), 2009−2015.
(37) Sheng, Y.; Tan, H.; Wang, X.; Warner, J. H. Hydrogen Addition for Centimeter-Sized Monolayer Tungsten Disulfide Continuous Films by Ambient Pressure Chemical Vapor Deposition. *Chem. Mater.* **2017**, *29* (11), 4904−4911.
(38) Meyer, B. Elemental sulfur. *Chem. Rev.* **1976**, *76* (3), 367−388.
(39) Wang, F.; Hwang, Y.; Qian, P. Z.; Wang, X. A statistics-guided approach to precise characterization of nanowire morphology. *ACS Nano* **2010**, *4* (2), 855−862.
(40) Li, Z.; Wang, F.; Kvit, A.; Wang, X. Nitrogen Doped 3D Titanium Dioxide Nanorods Architecture with Significantly Enhanced Visible Light Photoactivity. *J. Phys. Chem. C* **2015**, *119* (8), 4397−4405.
(41) Fei, L.; Lei, S.; Zhang, W. B.; Lu, W.; Lin, Z.; Lam, C. H.; Chai, Y.; Wang, Y. Direct TEM observations of growth mechanisms of two-dimensional MoS_2 flakes. *Nat. Commun.* **2016**, *7*, 12206.
(42) Bakti Utama, M. I.; Zhang, Q.; Zhang, J.; Yuan, Y.; Belarre, F. J.; Arbiol, J.; Xiong, Q. Recent developments and future directions in the growth of nanostructures by van der Waals epitaxy. *Nanoscale* **2013**, *5* (9), 3570−3588.
(43) Mohanty, D.; Lu, Z.; Sun, X.; Xiang, Y.; Wang, Y.; Ghoshal, D.; Shi, J.; Gao, L.; Shi, S.; Washington, M.; Wang, G.-C.; Lu, T.-M.; Bhat, I. Metalorganic chemical vapor epitaxy of very large CdTe grain size on mica through chemical and van der Waals interactions. *Physical Review Materials* **2018**, *2* (11), 113402.
(44) Mohanty, D.; Sun, X.; Lu, Z.; Washington, M.; Wang, G.-C.; Lu, T.-M.; Bhat, I. B. Analyses of orientational superlattice domains in epitaxial ZnTe thin films grown on graphene and mica. *J. Appl. Phys.* **2018**, *124* (17), 175301.
(45) Zheng, B.; Chen, Y.; Wang, Z.; Qi, F.; Huang, Z.; Hao, X.; Li, P.; Zhang, W.; Li, Y. Vertically oriented few-layered HfS_2 nanosheets: growth mechanism and optical properties. *2D Mater.* **2016**, *3* (3), 035024.
(46) Yang, Y. B.; Dash, J. K.; Littlejohn, A. J.; Xiang, Y.; Wang, Y.; Shi, J.; Zhang, L. H.; Kisslinger, K.; Lu, T. M.; Wang, G. C. Large Single Crystal SnS_2 Flakes Synthesized from Coevaporation of Sn and S. *Cryst. Growth Des.* **2016**, *16* (2), 961−973.
(47) Liang, H.; Shi, H.; Zhang, D.; Ming, F.; Wang, R.; Zhuo, J.; Wang, Z. Solution Growth of Vertical VS_2 Nanoplate Arrays for Electrocatalytic Hydrogen Evolution. *Chem. Mater.* **2016**, *28* (16), 5587−5591.
(48) Masikhwa, T. M.; Barzegar, F.; Dangbegnon, J. K.; Bello, A.; Madito, M. J.; Momodu, D.; Manyala, N. Asymmetric supercapacitor based on VS_2 nanosheets and activated carbon materials. *RSC Adv.* **2016**, *6* (45), 38990−39000.
(49) Liu, J.-Z.; Guo, P.-F. VS_2 nanosheets: A potential anode material for Li-ion batteries. *J. Inorg. Mater.* **2015**, *30* (12), 1339−1344.
(50) Patterson, A. L. The Scherrer Formula for X-Ray Particle Size Determination. *Phys. Rev.* **1939**, *56* (10), 978−982.
(51) Poddar, P.; Rastogi, A. K. Metastability and disorder effects in nonstoichiometric VS_2. *J. Phys.: Condens. Matter* **2002**, *14* (10), 2677−2689.
(52) Beal, A. R.; Liang, W. Y. Charge transfer in intercalation. *J. Phys. C: Solid State Phys.* **1973**, *6* (24), L482−L485.
(53) Guzman, D. M.; Onofrio, N.; Strachan, A. First principles investigation of copper and silver intercalated molybdenum disulfide. *J. Appl. Phys.* **2017**, *121* (5), 055703.
(54) Yang, C.; Ou, X.; Xiong, X.; Zheng, F.; Hu, R.; Chen, Y.; Liu, M.; Huang, K. V5S8−graphite hybrid nanosheets as a high rate-capacity and stable anode material for sodium-ion batteries. *Energy Environ. Sci.* **2017**, *10* (1), 107−113.
(55) Katsuta, H.; McLellan, R. B.; Suzuki, K. Physcio-chemical properties of the non-stoichiometric VS2 and V5S8 phases. *J. Phys. Chem. Solids* **1979**, *40* (12), 1089−1091.
(56) Yapsir, A. S.; Choi, C. H.; Lu, T. M. Observation of a new Al(111)/Si(111) orientational epitaxy. *J. Appl. Phys.* **1990**, *67* (2), 796−799.
(57) Zur, A.; McGill, T. C. Lattice match: An application to heteroepitaxy. *J. Appl. Phys.* **1984**, *55* (2), 378−386.
(58) Littlejohn, A. J.; Xiang, Y.; Rauch, E.; Lu, T. M.; Wang, G. C. van der Waals epitaxy of Ge films on mica. *J. Appl. Phys.* **2017**, *122* (18), 185305.
(59) Wang, Y.; Gao, L.; Yang, Y.; Xiang, Y.; Chen, Z.; Dong, Y.; Zhou, H.; Cai, Z.; Wang, G.-C.; Shi, J. Nontrivial strength of van der Waals epitaxial interaction in soft perovskites. *Physical Review Materials* **2018**, *2* (7), 076002.
(60) Li, H.; Qi, X.; Wu, J.; Zeng, Z.; Wei, J.; Zhang, H. Investigation of MoS_2 and graphene nanosheets by magnetic force microscopy. *ACS Nano* **2013**, *7* (3), 2842−2849.
(61) Rugar, D.; Mamin, H. J.; Guethner, P.; Lambert, S. E.; Stern, J. E.; McFadyen, I.; Yogi, T. Magnetic force microscopy: General principles and application to longitudinal recording media. *J. Appl. Phys.* **1990**, *68* (3), 1169−1183.
(62) Neves, C. S.; Quaresma, P.; Baptista, P. V.; Carvalho, P. A.; Araújo, J. P.; Pereira, E.; Eaton, P. New insights into the use of magnetic force microscopy to discriminate between magnetic and nonmagnetic nanoparticles. *Nanotechnology* **2010**, *21* (30), 305706.
(63) Feng, J.; Sun, X.; Wu, C.; Peng, L.; Lin, C.; Hu, S.; Yang, J.; Xie, Y. Metallic few-layered VS_2 ultrathin nanosheets: high two-dimensional conductivity for in-plane supercapacitors. *J. Am. Chem. Soc.* **2011**, *133* (44), 17832−17838.
(64) Feng, J.; Peng, L.; Wu, C.; Sun, X.; Hu, S.; Lin, C.; Dai, J.; Yang, J.; Xie, Y. Giant moisture responsiveness of VS_2 ultrathin nanosheets for novel touchless positioning interface. *Adv. Mater.* **2012**, *24* (15), 1969−1974.
(65) Samad, L.; Bladow, S. M.; Ding, Q.; Zhuo, J.; Jacobberger, R. M.; Arnold, M. S.; Jin, S. Layer-Controlled Chemical Vapor Deposition Growth of MoS_2 Vertical Heterostructures via van der Waals Epitaxy. *ACS Nano* **2016**, *10* (7), 7039−7046.
(66) Putsche, B.; Tumbek, L.; Winkler, A. The influence of potassium on the growth of ultra-thin films of para-hexaphenyl on muscovite mica(001). *J. Chem. Phys.* **2012**, *137* (13), 134701.

DOI: 10.1021/acsanm.9b00608
ACS Appl. Nano Mater. 2019, 2, 3684−3694